Elucidating the Origin of External Quantum Efficiency Losses in Cuprous Oxide Solar Cells through Defect Analysis

Jiantuo Gan†, Robert L. Z. Hoye‡, Yulia Ievskaya, Lasse Vines, Andrew T. Marin, Judith L. MacManus-Driscoll, and Edouard V. Monakhov**

Dr. J. Gan, Assoc. Prof. Lasse Vines, Prof. E. V. Monakhov
University of Oslo, Department of Physics/Center for Materials Science and Nanotechnology, P.O. Box 1048 Blindern, N-0316 Oslo, Norway
E-mail: edouard.monakhov@fys.uio.no
Dr. R. L. Z. Hoye, Dr. Y. Ievskaya, Prof. J. L. MacManus-Driscoll
Department of Materials Science and Metallurgy, University of Cambridge, 27 Charles Babbage Road, Cambridge, CB3 0FS, UK
E-mail: jld35@cam.ac.uk
Dr. A. T. Marin
Intel Corp.

Present Address
† School of Materials Science and Engineering, Xi'an Shiyou University, Xi'an 710065, People's Republic of China (J.G.)
‡ Department of Materials, Imperial College London, Exhibition Road, London SW7 2AZ, UK (R.L.Z.H.)

Keywords: Cuprous oxide solar cells; atmospheric pressure spatial atomic layer deposition; interface and bulk defects; impedance spectroscopy; quantum efficiency

Abstract: Heterojunction Cu_2O solar cells are an important class of earth-abundant photovoltaics that can be synthesized by a variety of techniques, including electrochemical deposition (ECD) and thermal oxidation (TO). The latter gives the most efficient solar cells of up to 8.1 %, but is limited by low external quantum efficiencies (EQE) in the long wavelength region. By contrast, ECD Cu_2O gives higher short wavelength EQEs of up to 90 %. We elucidate the cause of this difference by characterizing and comparing ECD and TO films using impedance spectroscopy and fitting with a lumped circuit model to determine the trap density, followed by simulations. The data indicates that TO Cu_2O has a higher density of interface defects, located approximately 0.5 eV above the valence band maximum (N_V), and lower bulk defect density thus explaining the lower short wavelength EQEs and higher long wavelength EQEs. This work shows that a route to further efficiency increases of TO Cu_2O is to reduce the density of interface defect states.

1. Introduction

Heterojunction solar cells with *p*-type Cu_2O (with a direct forbidden bandgap of 2.1 eV) are appealing because they are non-toxic, composed of Earth-abundant elements, and can be synthesized by a variety of techniques.[1-6] These techniques include electrochemical deposition (ECD) and thermal oxidation.[6-13] A variety of *n*-type buffer layers have been used, including ZnO,[7, 8, 10] zinc magnesium oxide ($Zn_{1-x}Mg_xO$),[6, 9, 10] amorphous zinc tin oxide,[1] zinc germanium oxide ($Zn_{1-x}Ge_xO$),[13] gallium oxide,[14] and aluminum gallium oxide.[12]

The theoretical power conversion efficiency of Cu_2O solar cells is expected to reach 18–23 %,[1, 4, 6, 8, 15] but experimental values currently vary between 1–8 %.[1, 6, 8, 9, 11, 13, 16] Losses can arise from non-radiative recombination centers or a limited minority carrier collection length.[17, 18] Non-radiative recombination centers include crystallographic defects, impurities or other carrier traps (in the bulk or at the interfaces). These defects can affect the open-circuit voltage (V_{OC}), fill factor (FF) and short circuit current density (J_{SC}).[19] Interfacial defects can exist in the form of layers or 'islands' of CuO (cupric oxide) from different processing methods,[4, 6, 20, 21] or they can originate from the lattice mismatch at the hetero-interface.[22, 23] Bulk defects can originate from contaminants in the electrodeposition solution, structural defects (*e.g.*, grain boundaries or stacking faults) or intrinsic defects, such as copper vacancies.[24, 25] On the other hand, the minority carrier collection length depends on the mobility and its carrier lifetime of the Cu_2O.[18] Thermally oxidized (TO) films tend to have higher mobilities due to larger grains,[12, 26, 27] resulting in longer minority carrier collection lengths.[14] As a result, TO Cu_2O has larger long wavelength EQEs than ECD Cu_2O, with longer diffusion length (300–400 nm in the TO samples *vs*. 160 nm in ECD samples[18, 28]).[6, 14] However, TO Cu_2O solar cells are limited by a low EQE at short wavelengths (375–490 nm),[6, 12] whereas ECD Cu_2O solar cells have EQEs of 80 % or larger in this region.[14, 26] Understanding the reason for this difference is important to achieve future efficiency improvements.

To study the differences in EQE, $Cu_2O/Zn_{0.8}Mg_{0.2}O$ heterojunction (HJ) solar cells were made. The Cu_2O was fabricated by both TO and ECD, while the $Zn_{0.8}Mg_{0.2}O$ buffer layer was deposited on top by AP-CVD using previously reported conditions.[6, 9] In AP-CVD, the metal precursor and oxidant gas channels are separated with inert gas barriers, enabling the two half-reactions in ALD to occur under atmospheric pressure, with an order of magnitude higher growth rate than standard ALD.[3] We have found AP-CVD to be highly advantageous for rapidly depositing pinhole-free, thin (10–200 nm) oxide buffer layers for both ECD and TO Cu_2O solar cells.[6, 9]

We characterized these devices by impedance spectroscopy and developed an equivalent lumped circuit model to analyze and compare differences in interfacial and bulk traps. In the model, a pair of resistors and capacitors were used in series to simulate the electrical response of active defects located both in the bulk and at the interface, and the differential capacitance $\omega \cdot dC/d\omega$ was used to determine the trap density from frequency sweeps in impedance spectroscopy. By comparing the traps in ECD Cu_2O to TO Cu_2O, we conclude that TO Cu_2O exhibits a higher density of interface traps. Through SCAPS simulations, we confirmed that this correlates with a reduced short wavelength EQE. We determine that further efficiency improvements to ECD Cu_2O heterojunctional solar cells could come about by improve interface with less interface defect recombination.

2. Results and Discussion

2.1. Developing a lumped circuit model of Cu_2O-$Zn_{1-x}Mg_xO$ solar cells

A lumped resistor-capacitor (RC) circuit (Figure 1a) can be established to describe the electrical response of a complete *p-n* junction (including metal-semiconductor junctions).[29, 30] For the $Cu_2O/Zn_{0.8}Mg_{0.2}O$ HJ in the current study, the circuit is comprised of two types of junctions: (1) the *p-n* junction (between $Cu_2O/Zn_{0.8}Mg_{0.2}O$) and (2) two metal-semiconductor junctions, Ag/ITO/Al doped ZnO (AZO)/$Zn_{0.8}Mg_{0.2}O$ and Cu_2O/Au (or Cu_2O/ITO for the anode of ECD Cu_2O). In Figure 1a, R_{nc} and R_{pc} are the contact resistances for Ag/ITO/(AZO)/$Zn_{0.8}Mg_{0.2}O$ and Cu_2O/Au (or Cu_2O/ITO) junctions, respectively. Dynamic resistance and capacitance associated with surface states at the metal-semiconductor interface are denoted by R_{ns} and C_{ns} for Ag/ITO/(AZO)/$Zn_{0.8}Mg_{0.2}O$, R_{ps} and C_{ps} for Au/Cu_2O (or Cu_2O/ITO). In order to analyze the depletion region of the HJ, the circuit was divided into an infinite number of small segments by geometry and each segment (i.e. the *i*th segment) consists of resistors and capacitors connected in parallel (ΔC_i and ΔR_i) and series (ΔC_{ti} and ΔR_{ti}). In the $Cu_2O/Zn_{0.8}Mg_{0.2}O$ HJ, Cu_2O (*p*-type, $N_A \approx 10^{14}$–10^{15} cm^{-3})[17] is usually ~2–4 orders of magnitude lower than $Zn_{0.8}Mg_{0.2}O$ (*n*-type, N_D =~10^{17}–10^{19} cm^{-3}),[9, 17] forming an abrupt heterojunction, see Figure 1b. As a result, ΔC_i and ΔR_i in Figure 1a are geometry related elements and can be expressed by Equations 1a&b,[29] while ΔC_{ti} and ΔR_{ti} are dynamic (or defect) related elements and can be expressed by Equations 1a&d:[31]

$$\Delta C_\mathrm{i} = \frac{\varepsilon}{\Delta x} \quad (1a)$$

$$\frac{1}{\Delta R_\mathrm{i}} = \Delta G_\mathrm{i} = \frac{\sigma}{\Delta x} \quad (1b)$$

$$\Delta C_\mathrm{ti} = q^2 N_t(x)\Delta x \quad (1c)$$

$$\frac{1}{\Delta R_\mathrm{ti}} = \Delta G_\mathrm{ti} = \frac{\Delta C_\mathrm{ti}}{\tau_\mathrm{t}(x)} \quad (1d)$$

In Equations 1a&b, ε and σ are the dielectric constants and conductivity of Cu_2O respectively. Δx is the thickness of the ith segment. In Equation 1c, N_t is denoted as the trap density, q the electron charge and ΔC_{ti} the capacitance associated with a certain trap, which models the capture and emission of carriers from the trap. The conductance of the trap, ΔG_{ti}, can be related to ΔC_{ti} by Equation 1d, where τ_t is the time constant of a trap and the reciprocal of its angular frequency, ω. As a result, elements associated with traps are frequency dependent. The relation between frequency and energy levels can be expressed by Equation 2a:[17]

$$\omega(E_\omega) = \frac{2\pi}{\tau_t(E_\omega)} = 2\pi\left(\sigma_i v_{th} N_V\right)e^{-E_\omega/kT} \qquad (2a)$$

$$\omega_o = \omega(E_o) = 2\pi\left(\sigma_j v_{th} N_V\right)e^{-E_o/kT} \qquad (2b)$$

In Equations 2a&b, σ_j is the capture cross-section of a trap, v_{th} the thermal velocity, N_V the density of states at the Cu_2O valence band, E_ω the corresponding energy position at x_ω (Figure 1a). $\omega(E_\omega)$ in Equation 2a has an inverse exponential relationship with E_ω. The angular frequency, ω, can therefore be expressed as the corresponding trap frequency, ω_o, when the energy level, E_ω, is equal to E_o for a bulk defect level at the location x_o (Equation 2b). In Equations 2a&b, σ_j is the capture cross-section of a trap, v_{th} the thermal velocity, N_V the density of states at the Cu_2O valence band, E_ω the corresponding energy position at x_ω (Figure 1a). $\omega(E_\omega)$ in Equation 2a has an inverse exponential relationship with E_ω. The angular frequency, ω, can therefore be expressed as the corresponding trap frequency, ω_o, when the energy level, E_ω, is equal to E_o for a bulk defect level at the location x_o (Equation 2b).

Before establishing the theoretical model, three approximations were made:

(1) Contact resistances (R_{nc}, R_{pc}) were neglected here even if a small Schottky barrier exists for both types of solar cells, with the one in the ECD Cu_2O sample being more significant (Nyquist plots in Figure S1). This approximation is valid because, in the model, these two parameters are associated in the circuit in a parallel fashion, which makes it constant in the differential capacitance measurement;

(2) For simplicity, surface states at the metal-semiconductor junctions (R_{ns} and C_{ns} for Ag/ITO/AZO/$Zn_{0.8}Mg_{0.2}O$, R_{ps} and C_{ps} for Au/Cu_2O) were neglected.[29] These parameters are slow reacting in comparison to that from the bulk and interface of the device, reflected by the distance from the hetero-interface. In the measurement, the lowest frequency was ~10^2 rad/s, making it less possible for detecting the influence of two slow reacting regions;

(3) The dimension-related elements for ZnO, R_n and C_n, were ignored. This is valid because $Cu_2O/Zn_{0.8}Mg_{0.2}O$ is an abrupt heterojunction.[17, 29]

In the equivalent circuit model (Figure 1a), the frequency response of traps to carriers affects whether a group of electrical elements should be incorporated in parallel to the previous circuit, i.e., whether ΔR_i and ΔC_i are connected in parallel to ΔR_{ti} and ΔC_{ti}.

Therefore, the admittance relation between $Y_{\mathrm{pn}}(x + \Delta x)$ and $Y_{\mathrm{pn}}(x)$ can be formulated as Equation 3.[32]

$$Y_{pn}(x+\Delta x) = \frac{1}{Z_{pn}(x+\Delta x)} = \frac{1}{\dfrac{1}{Y_{pn}(x)} + \dfrac{1}{j\omega \Delta C_{ti}} + \dfrac{1}{\Delta G_{ti}}} \qquad (3)$$

In Equation 3, $Z_{\mathrm{pn}}(x + \Delta x)$ is the impedance of the *p-n* junction. Inserting Equations 1a-d into Equation 3 yields Equation 4a. The calculation details can be found in Figure S2 of the supporting information (SI):

$$\frac{dY_{pn}}{dx} = -\frac{Y_{pn}^{\,2}(x)}{j\omega\varepsilon + \sigma} + \frac{j\omega q^2 N_t}{1 + j\omega\tau_t} \qquad (4a)$$

By inserting Equations S3-S7 into Equation 4a from Figure S3:

$$-\frac{\omega}{\lambda}\frac{dY_{pn}}{d\omega} = -\frac{Y_{pn}^{\,2}(x)}{j\omega\varepsilon + \sigma} + \frac{j\omega q^2 N_t}{1 + j\omega\tau_t} \qquad (4b)$$

where λ is an attenuation factor ($\lambda = -kTL_{\mathrm{o}}/\Delta E_{\omega}$). The admittance consists of real and imaginary components, namely, $Y_{\mathrm{pn}} = G_{\mathrm{pn}} + jB_{\mathrm{pn}}$ and thus can be projected for the two components for the *p-n* junction.

$$\frac{dB_{\mathrm{pn}}}{d\omega} = \frac{\lambda}{\omega}\left(\frac{2G_{\mathrm{pn}}B_{\mathrm{pn}}\sigma - \omega\varepsilon\left(G_{\mathrm{pn}}^{\;2} - B_{\mathrm{pn}}^{\;2}\right)}{\sigma^2 + \omega^2\varepsilon^2} - \frac{\omega q^2 N_{\mathrm{t}}}{1 + \omega^2\tau_{\mathrm{t}}^{\,2}}\right) \qquad (5a)$$

$$\frac{dG_{\mathrm{pn}}}{d\omega} = \frac{\lambda}{\omega}\left(\frac{\sigma\left(G_{\mathrm{pn}}^{\;2} - B_{\mathrm{pn}}^{\;2}\right) + 2G_{\mathrm{pn}}B_{\mathrm{pn}}\omega\varepsilon}{\sigma^2 + \omega^2\varepsilon^2} - \frac{\omega q^2 N_{\mathrm{t}}\tau_{\mathrm{t}}}{1 + \omega^2\tau_{\mathrm{t}}^{\,2}}\right) \qquad (5b)$$

Further, replacing B_{pn} with ωC_{pn} in Equation 5a, and by rearranging Equation 5a so that $N_{\mathrm{t}}(C)$ is the subject the trap density, $N_{\mathrm{t}}(C)$, can be obtained. At the same time, the subscript *p-n* for *G*, *B* and *C* are removed for convenience and Equations 6 are obtained:

$$N_{\mathrm{t}}(C) = \frac{1 + \omega^2\tau_{\mathrm{t}}^{\,2}}{\omega q^2}\left(\frac{2G\,\omega C\sigma - \omega\varepsilon\left(G^2 - \omega^2 C^2\right)}{\sigma^2 + \omega^2\varepsilon^2} - \frac{\omega\Delta E_{\omega}}{kTL_{\mathrm{o}}}\left(\omega\frac{dC}{d\omega} + C\right)\right) \qquad (6a)$$

$$N_{\mathrm{t}}(G) = \frac{1 + \omega^2\tau_{\mathrm{t}}^{\,2}}{\omega^2 q^2\tau_{\mathrm{t}}}\left(\frac{\sigma\left(G^{\,2} - \omega^2 C^2\right) + 2GC\omega^2\varepsilon}{\sigma^2 + \omega^2\varepsilon^2} - \frac{\omega\Delta E_{\omega}}{kTL_{\mathrm{o}}}\frac{dG}{d\omega}\right) \qquad (6b)$$

$N_{\mathrm{t}}(C)$ is related to the differential capacitance, $\omega\cdot\mathrm{d}C/\mathrm{d}\omega$, by the second term in Equation 6a. $N_{\mathrm{t}}(G)$ can be related to the differential conductance G in Equation 6b, but further discussion is beyond the scope of this paper.

In Figure 1b, the Fermi level (E_{F}) intersects with both interface defects and the bulk trap level (E_{T}), numbered 1 and 2 respectively. Both types of defects can affect the results of admittance spectroscopy. In order to differentiate interface defects from bulk defects, admittance measurements should be performed at different biases to determine how the differential capacitance, $\omega \cdot dC/d\omega$, is affected.[33] In Figure 1b, the bulk defect level (E_T) is in general energetically discrete and the energy difference (ΔE_o) is bias independent. Conversely, the interface defects are continuous and the energy difference (E_{fpi}) is bias dependent,[33] which is defined as:

$$E_{\mathrm{fpi}} = E_{\mathrm{fp}\infty} + q(V_{bi} - V) \qquad (7)$$

Consequently, the peak of $\omega \cdot dC/d\omega$ from admittance measurements will shift under different biases for interface defect states. Equation 6a describes N_t for bulk defects. In order to calculate the trap density for interface defects, Equation 8 from the literature can alternatively be used as a simple approach:[33]

$$N_{it} = -\frac{2}{q^2}\omega\frac{dC}{d\omega} \quad (8)$$

In Equation 8, the differential capacitance, $\omega \cdot dC/d\omega$, is also used for trap density calculations in a similar way to Equation 6a.

To determine the trap density for bulk defects, N_t, of the heterojunction, Equation 6a can be solved numerically. In the current study, the Ordinary Differential Equation (ODE) function in MATLAB® was used. Before solving Equation 6a, some important parameters needed to be estimated or calculated from the literature, i.e., Debye length, thermal velocity, trap capture cross-section, thickness distribution of the depletion region at each side of the HJ. Initial conditions, such as N_t and trap energy level, are also needed to numerically solve the differential equations. Here, the first term in Equation 6a according to the above mentioned numerical analysis does not obviously change the capacitance of the *p-n* junction and thus can be removed from the equation, at the same time *C* in the second term is removed for the same reason, resulting in a reduced form as Equation 9:[30, 33]

$$N_{\mathrm{t}} = -\frac{\Delta E_{\omega}}{kTL_{\mathrm{o}}}\frac{1+\omega^2\tau_{\mathrm{t}}^2}{q^2}\omega\frac{dC}{d\omega} \qquad (9)$$

Below is an example of the result from the numerical analysis. In the bias dependent measurements (Figures 2a-b), the peaks of the differential capacitance $\omega \cdot dC/d\omega$ are plotted against the angular frequency under different applied biases (from –0.5 to 0.5 V). For bulk traps (Figure 2a), the peaks at each bias are plotted in such a way that they align at one frequency ($\omega = 1.7\times10^4$ rad·s^{-1}) depending on the bulk trap energy level above E_V. The intensity of peaks increases from reverse to forward bias. The exception is for 0.5 V forward bias, where the $\omega \cdot dC/d\omega$ peak is absent because the probing energy, E_ω, would otherwise be smaller than E_{VF} at the highest frequency (Figure 1b), which is physically impossible. The increase in peak intensity from reverse to forward bias indicates a higher bulk trap density at larger bias as a result of the trap density being proportional to $\omega \cdot dC/d\omega$ (Equation 9). This is reasonable because the capture cross-section between the trap level and Fermi level is larger with the lower band bending under forward bias (Figure 1b). By contrast, for interface defects (Figure 2b), the peaks shift evenly from low to high frequencies for applied biases between –0.1 V and 0.1 V. This peak shift is due to ΔE_ω is being highly influenced by the external applied voltage for interface defects, as reflected by the voltage dependence of E_{fpi} (Eq. 7). Whereas for the bulk defects, ΔE_ω remains constant because the applied bias does not change the bulk trap energy level.

In Figure S1c, the differential capacitance $\omega \cdot dC/d\omega$ shifts its peak position in angular frequency, ω, (from 1.2×10^5 to 1.7×10^4 rad·s^{-1}) with increasing temperature (from 22 ºC to 72 ºC). The main reason for the shifts can be explained by Equation 2b, where the angular frequency of a trap (ω_o) is dependent on the thermal energy, kT. In order to extract ΔE_o (bulk trap energy level above N_V) from Figure S1c, the results of $\ln(\omega_o)$ and $(kT)^{-1}$ are obtained and summarized in Table 1. Rewriting Equation 2b, Equation 10 can be obtained:

$$\ln(\omega_o) = -\frac{\Delta E_o}{kT} + \ln(2\pi\sigma_j v_{th} N_V) \qquad (10)$$

As a result, the Arrhenius plot can be made based on the temperature-dependent measurements (Figure 2d), with ΔE_o as the slope of the $\ln(\omega_o)$ and $(kT)^{-1}$ plot.

In order to determine ΔE_o, Equation 6a can again be solved numerically with an initial value of trap energy, 0.45 eV from the valance band, as obtained from the literature,[17] so that under different temperatures (22–72 °C), the differential capacitance can be plotted with frequency in Figure 2c. Further, values of ln (ω_o) and $-1/kT$ are extracted from Figure 2c, and are listed in Table 1 and displayed in Figure 2d, so that ΔE_o can be extracted. The extracted ΔE_o is ~0.43±0.01 eV and agrees well with the initial value. This actually further indicates the validity of Equation 6a for trap density determination. The difference of 0.02 eV between the value obtained by fitting the measurements and the literature value can be considered as numerical errors in the simulation (given that kT is 0.025 eV). The measurements at different temperatures is also complicated by the heating of the Cu_2O and possible formation of CuO at the heterojunction at above 50 ºC during the growth of the $Zn_{0.8}Mg_{0.2}O$ layer.[10] As a result, we will focus on the bias-dependent measurements in this work. We have therefore developed the necessary analytical techniques and methodology for measuring the defect states present in our $Cu_2O/Zn_{1-x}Mg_xO$ HJs.

2.2. Performance of $Cu_2O/Zn_{0.8}Mg_{0.2}O$ solar cells

We made test on devices from both TO and ECD Cu_2O. The J–V curves measured under 1 sun AM 1.5G illumination is shown in Figure 3a. From these, the performance parameters were calculated and shown in Table 2. We have previously found the optimal deposition temperature for $Zn_{0.8}Mg_{0.2}O$ is with thermally oxidized Cu_2O underlayer being held at 150 °C,[6] which we used here. For comparison, we also deposited $Zn_{0.8}Mg_{0.2}O$ with ECD Cu_2O (ECD05) at 150 °C. On the other hand, we have previously found the device performance to be improved at lower deposition temperatures (80 °C).[9] Hence, we also used this lower deposition temperature for the fabrication of a further ECD sample, ECD03. Irrespective of Cu_2O deposition methods using TO or ECD, we have obtained a final PCE of approximately 1% in both of the Cu_2O devices. But their contributions are quite different. For ECD03 Cu_2O sample, it has a higher FF (53%) but it has a lower J_{SC} (4.4 mA·cm^{-2}), in comparison with those of 35% and 8.5 mA·cm^{-2} in the TO Cu_2O sample. Typically, the difference of the contributions to the PCEs for the ECD and TO Cu_2O samples suggests that the recombination mechanisms are not the same, which we will further compared the wavelength dependent measurement setup.

Despite the comparable efficiencies, the TO and ECD Cu_2O devices had different EQEs (Figure 3b). Whereas the TO Cu_2O had a higher EQE in the long wavelength range (490–600 nm), its EQE dips by approximately 20 % at wavelengths between 400 nm and 490 nm, consistent with previous reports.[6, 12] By contrast, the EQE of the ECD Cu_2O reached ~90% in the short wavelength range, even for ECD05 (Figure 3b). In order to clarify the differences in the EQE results, the drift-diffusion model by Musselman *et al.*[18] was used to model the charge transport length in both types of devices. The results showed than the diffusion length of minority carriers in the TO sample is 310 nm, three times of that of the ECD sample. Consequently, this leads to a large EQE at long wavelengths. Our results agree well with the diffusion lengths obtained from earlier studies. However, the efficiency of the TO sample is still limited by a poor hetero-interface,[6] even though it has a longer drift length of minority charge carriers (2790 nm) than the ECD sample (110 nm drift length).[18] Musselman *et al.*[18] was successful in using the drift-diffusion model to determine the charge transport diffusion for TO and ECD samples. On the other hand, the underlying mechanisms and the fundamental reasons for the difference between the two samples were not explored. On the other hand, Marin *et al.*[33] introduced admittance spectroscopy as a means to determine the trap density of hetero-interfaces in Cu_2O based PV solar cells. But they did not differentiate between the two major recombination pathways. In particular, the reason for the low short wavelength EQE in thermally oxidized Cu_2O device was not determined. To answer these questions, in this work, we established a lumped circuit model to differentiate the effects of interface and bulk detects on efficiency losses in these two samples.

2.3. Defect analysis of $Cu_2O/Zn_{0.8}Mg_{0.2}O$ heterojunctions

A lumped circuit model with impedance spectroscopy was used to analyze TO and ECD samples (ECD03 and ECD05, respectively, with more details on impedance analysis of ECD05 shown in Figure S4). In the Nyquist plots for the two types of samples, the imaginary component of the impedance (–*Z*'') is plotted against the real component (*Z*') under an applied D.C. bias of –0.5 V to 0.5 V. The Nyquist plots are depressed semicircles at each D.C. bias, in which the center is below the *Z*' axis (i.e., –*Z*'' < *Z*' at the maximum for –*Z*''), which indicates that a defect-related impedance component should be added to the model.[33] A separate small semicircle was also present in the low impedance region for both types of samples. But for the TO Cu_2O, the smaller semicircle merged into the larger semicircle (Figure S1b'), indicating that Schottky contacts have less of an influence than for ECD03 (Figure S1a').

Analyzing the differential capacitance plots gives an indication of the defect states present. For ECD03 (Figure 4a), there is only one differential capacitance peak at each D.C. bias and the peak intensity showed a slight increase with applied biases from –0.5 V to 0.3 V, but then reduced to a lower intensity at a bias of 0.5 V. At the same time, the peak position shifted from 3.7×10^4 rad·s^{-1} to 2.7×10^5 rad·s^{-1} with increasing D.C. bias. In a first approximation, the bias dependent differential capacitance for the ECD sample may seem to have followed the trend of interface defects. However, the magnitude of the bias dependent peak indicated in Figure 2b for interface defects shows a strong shift in frequency within a voltage range of –0.1 V to 0.1 V. Hence, the experimental peak shift in the ECD sample does not seem to match the characteristics of interface defects. Because a small shift in these peaks means little variation of trap energy, formulated by Equation 2a, where frequency is related to the energy, contradicting the nature of continuous energy distribution of the interface traps (0.4–0.8 eV above valance band).[17] Using this equation, however, the peak shift in the ECD sample indicated a bias dependent trap energy (E_o) of ~0.44–0.48 eV, with trap energy of 0.46 eV for zero bias. If bulk defects are allowed to vary within a certain range, e.g., due to its density distribution with energy, or formation of bulk defects in band, with external bias, then it is reasonable to attribute these peaks to bulk defects. Indeed, a defect band was observed in as-deposited Cu_2O film and was claimed as the main reason for difference in optical absorption.[34] Therefore, it is surmised that the peak shifting in the ECD sample is caused by a band defect and the bulk defects are located 0.46 ±0.02 eV above E_V. This agrees with early observation of trap density at 0.475 eV for Cu_2O from deep level transient spectroscopy (DLTS).[35] Further, assignment of the peaks to bulk defects hinges on observation of long wavelength EQE loss in ECD sample.

From the differential capacitance plots for the thermally oxidized Cu_2O device (Figure 4b), the angular frequency (ω_o, aligned at 1.2×10^4 rad·s^{-1}) was unchanged with applied bias. In contrast, the peak intensity increased with applied biases of –0.5 V to 0.3 V, before dropping at 0.5 V. Again, according to the bias dependent feature of the differential peaks, the alignment of peaks for frequency can thus be tentatively assigned to bulk defects. However, the peak intensity in the thermally oxidized sample does not increase by the same magnitude as it does from the bulk defects (in Figure 2a), thus not reflecting the effect of band bending in defect activity with external biases. In fact, both the *J–V* and EQE measurements (Figure 3) suggest that interface defects played important roles for the thermally oxidized Cu_2O device. If so, one possibility for the absence of peak shifts with external bias in this device is that a large density of interface defects can pin the Fermi level and prevent the shift of the differential capacitance peaks under applied bias.[33] At interfaces, traps can be generated as a result of, e.g., dangling bonds or strain induced formation of CuO.[21] Fermi level pinning occurs when a particular vacancy or interstitial accumulates at the surface, resulting in the localization of these defects in energy.[33] The pinning of the Fermi level may result in lower band-bending at the heterojunction, resulting in a smaller built-in voltage, which may contribute to the lower V_{OC} of the thermally oxidized Cu_2O device (Table 2), and further the observed dip in EQEs at the short wavelength. We note that the thermally oxidized sample, which a V_{OC} of 0.336 V is much lower than that (0.43 V) of the ECD sample. At this moment, therefore, the peaks at ω_o~10^4 rad·s^{-1} for the thermally oxidized Cu_2O is assigned to pinned interface defects with $E_{fpi} \approx 0.5$ eV above E_V.[17] Further information is discussed in Sec. 2.4.

We also note that, in the thermally oxidized sample, there is a differential capacitance shoulder located at ω_o~10^6 rad·s^{-1} (Figure 4b) with lower intensity, and its intensity becomes larger at forward biases. Using Equation 2a, the corresponding energy level of the shoulders is ~0.27 eV above the N_V. This shoulder is mostly probably related to the inhomogeneity at the heterojunction, rather than a perturbation by a Schottky barrier.[17, 33] The inhomogeneity can cause varying profiles of energy level for defects. The appearance of such a shoulder is a characteristic feature of interface defects. In addition, as stated in Sec.2.1, items (1) and (2) resistances at the metal/semiconductor contact are ignored for simplicity and thus in the simulation results, Fig.2b&c, there is no trace of such small peaks. In addition, surface defects will affect both the simulation and experimental results at low frequencies because they are further away from the hetero-interface.

The trap density, calculated from Equation 8 (interface defects) and 9 (bulk defects) with our measurements, is shown in Figure S5. The thermally oxidized Cu_2O has interface defects with a peak in trap density at ~0.5 eV above E_V (Figure 6a). At the same time, the interface defect shows a variation in energy level to 0.27 eV due to inhomogeneity in the Cu_2O films. On the other hand, the ECD Cu_2O has a band of bulk defects located 0.46 ± 0.02 eV above E_V (Figure S5b). The distributed bulk defects in the ECD Cu_2O may arise from the higher density of grain boundaries than in the thermally oxidized Cu_2O, which can act as bulk recombination centers.[6, 9, 18] The trap density in the ECD Cu_2O is also an order of magnitude higher than the interface trap density in the thermally oxidized sample, which could be another reason why the ECD Cu_2O samples have lower long wavelength EQEs (Figure 3b). For sample ECD05, the differential capacitance peaks align at 6.1×10^4 rad/s for bias voltages varying from –0.5 V to 0.5 V (Figure S4c). This fits well with the simulated results, see Figure 2a, in terms of the alignment of peaks with external biases. Thus, this indicates that the defects are located at a fixed energy level, rather than an energy band for the ECD03 sample. On the other hand, the intensity of these peaks does not change with bias, indicating a uniform trap density. As a result, in comparison with the ECD03 sample, the ECD05 sample shows bulk defects with single energy level at 0.31 eV above N_V.

2.4. Simulations on the influence of interface recombination velocity on EQE

We performed simulations on the $Cu_2O/Zn_{0.8}Mg_{0.2}O$/AZO stack using SCAPS.[36] Using these simulations, we were able to determine the correlation between the defect

states we measured and the EQE. For thermally oxidized Cu_2O, we modeled the defects as interface states with a Gaussian distribution centered 0.5 eV above E_V. We compared the EQEs at different trap densities (N_t). When there are no interfacial traps, the EQE is 100% for wavelengths below 490 nm (Figure 7a). When the trap density increases to 2×10^{12} $eV^{-1} \cdot cm^{-2}$ (the same as the N_t measured for ECD Cu_2O), the EQE decreases in the short wavelength range. But with the trap density measured for thermally oxidized Cu_2O (2×10^{13} $eV^{-1} \cdot cm^{-2}$), the simulated EQE was 0%. Simulated EQEs are 0% for trap densities higher than 5.24×10^{12} $eV^{-1} \cdot cm^{-2}$.
We modeled ECD Cu_2O as having a Gaussian distribution of bulk defects centered 0.46 above E_V and no interface defects. In this case, the long wavelength EQEs are lower than those for thermally oxidized Cu_2O (Figure 5), and the short wavelength EQEs are 100 % for wavelengths below 490 nm. The trend in long wavelength EQEs is in agreement with our measurements (Figure 3b). We took the series resistance (20 $\Omega.cm^2$) and shunt resistance (300 $\Omega \cdot cm^2$) of the device into account in our simulations, but our short wavelength EQEs for ECD Cu_2O may not reach 100 % due to losses in the $Zn_{0.8}Mg_{0.2}O$ layer,[37] which we did not take to account for simplicity. We also considered the case where the 2×10^{12} $eV^{-1} \cdot cm^{-2}$ density of bulk defect states in ECD Cu_2O also occurred at the interface. This again resulted in a decrease in the short wavelength EQEs (Figure 5b). Our simulations are therefore consistent with our defect analysis that indicates that the lower short wavelength EQEs for thermally oxidized Cu_2O are a result of interfacial defect states.

3. Conclusion

We have analyzed defects in Cu_2O made by thermal oxidation (TO) and electrochemical deposition (ECD) by developing a lumped circuit model in impedance spectroscopy measurements. These show that TO Cu_2O predominantly has interfacial defect states centered 0.5 eV above E_V, whereas ECD Cu_2O predominantly has bulk states centered between 0.46 ± 0.02 eV above E_V. Through SCAPS simulations, we found that Cu_2O with predominantly interfacial rather than bulk defect states has higher long wavelength EQEs but lower short wavelength EQEs. This strongly agrees with our EQE measurements of TO and ECD Cu_2O heterojunction solar cells. This work indicates that the route to further improvements in Cu_2O solar cells is by defect control with interface engineering of the TO Cu_2O devices.

4. Experimental Section

Cu_2O synthesis: For thermally oxidized cuprous oxide, Cu_2O substrates were obtained by a 2 hour oxidation of 0.25 mm thick copper foil, finished by quenching of the substrates, as described in Ref.[6] The oxygen partial pressure was monitored throughout the heat treatment keep the substrates in the phase region where cuprous oxide is thermodynamically stable.[24] Cupric oxide (CuO) formed on the substrate surface during quenching was removed by etching. Substrates were then masked on

one side with insulating black paint, defining the solar cell area to be approximately 0.1 cm^2.

Electrochemically deposited (ECD) Cu_2O solar cells were prepared on ITO/glass using a previously reported method.[9] ITO/glass substrates were cleaned by scrubbing with 10 vol.% HCl, followed by ultrasonically cleaning for 15 minutes in water, toluene and isopropanol. Cu_2O was deposited at 40 °C from a solution of 0.2 $mol·L^{-1}$ Cu^{2+} (from $CuSO_4·5H_2O$), 1.5 $mol·L^{-1}$ lactic acid and ~2 $mol·L^{-1}$ OH^- (from NaOH) to keep the pH at 12.65. The current density was kept constant at –1.5 $mA·cm^{-2}$.

AP-CVD buffer layer deposition: $Zn_{0.8}Mg_{0.2}O$ was deposited on top of the Cu_2O by atmospheric pressure chemical vapor deposition (AP-CVD).[2] Diethylzinc and bis (ethylcyclopentadienyl) magnesium were used as the Zn and Mg precursors respectively, and deionized water was used as the oxidant source. Nitrogen gas was used to bubble through the precursors at 6 $mL·min^{-1}$ (Zn precursor), 200 $mL·min^{-1}$ (Mg precursor) and 100 $mL·min^{-1}$ (water). The metal precursors were diluted with nitrogen gas flowing at 100 $mL·min^{-1}$, and the oxidant diluted with nitrogen gas flowing at 200 $mL·min^{-1}$. These were fed to a gas manifold, along with nitrogen gas flowing at 500 $mL·min^{-1}$, to create separate channels of metal precursor and oxidant separated by channels of inert nitrogen gas. 600 oscillations of the substrate beneath the gas manifold was used, giving films of approximately 60 nm in thickness.

Characterization: An Agilent 4294 Precision Impedance Analyzer was used to characterize the impedance spectra against the normal frequency in Hz. The measurement was performed at a certain applied bias voltage with AC signal (amplitude of 20 mV, sweeping from 40 Hz to 10 MHz). The temperature was controlled by using a hotplate and was monitored by a thermocouple. The samples were stored in the darkness for the same period of time (overnight) prior to the experiments in order to empty the traps that became occupied upon light soaking.

Solar simulations were performed under AM 1.5G radiation using an Oriel 92250A solar simulator according to previous reports.[6, 9] External quantum efficiency measurements were performed using a 100 W tungsten halogen lamp source and monochromator, according to previous reports.[6]

Acknowledgements

The work is dedicated to Professor Bengt Gunnar Svensson, who was supervisor of J.G. during his Ph.D. thesis study and unfortunately passed away due to heart attack in June 2018 before the manuscript was submitted. This work was conducted under the research project ***Development of a Hetero-Junction Oxide-Based Solar Cell Device (HeteroSolar)***, financially supported by the Research Council of Norway (RCN) (research project ES483391 with number:-1) through the RENERGI program. The authors also acknowledge the support of the Cambridge Overseas and Commonwealth

Trust, the Rutherford Foundation of New Zealand, and the ERC Advanced Investigator Grant, Novox, ERC-2009-adG247276.

References

[1] Y.S. Lee, J. Heo, S.C. Siah, J.P. Mailoa, R.E. Brandt, S.B. Kim, R.G. Gordon, T. Buonassisi, Energy Environ. Sci., 6 (2013) 2112-2118.
[2] R.L. Hoye, D. Muñoz-Rojas, K.P. Musselman, Y. Vaynzof, J.L. MacManus-Driscoll, ACS Appl. Mater. Interfaces, 7 (2015) 10684-10694.
[3] R.L. Hoye, D. Muñoz-Rojas, S.F. Nelson, A. Illiberi, P. Poodt, F. Roozeboom, J.L. MacManus-Driscoll, APL Mater., 3 (2015) 040701.
[4] S.S. Wilson, J.P. Bosco, Y. Tolstova, D.O. Scanlon, G.W. Watson, H.A. Atwater, Energy Environ. Sci., 7 (2014) 3606-3610.
[5] S. Ruhle, A.Y. Anderson, H.-N. Barad, B. Kupfer, Y. Bouhadana, E. Rosh-Hodesh, A. Zaban, The Journal of Physical Chemistry Letters, 3 (2012) 3755-3764.
[6] Y. Ievskaya, R. Hoye, A. Sadhanala, K. Musselman, J.L. MacManus-Driscoll, Sol. Energy Mater. Sol. Cells, 135 (2015) 43-48.
[7] K.P. Musselman, A. Wisnet, D.C. Iza, H.C. Hesse, C. Scheu, J.L. MacManus-Driscoll, L. Schmidt-Mende, Adv. Mater., 22 (2010) E254-E258.
[8] T. Gershon, K.P. Musselman, A. Marin, R.H. Friend, J.L. MacManus-Driscoll, Sol. Energy Mater. Sol. Cells, 96 (2012) 148-154.
[9] R.L. Hoye, S. Heffernan, Y. Ievskaya, A. Sadhanala, A. Flewitt, R.H. Friend, J.L. MacManus-Driscoll, K.P. Musselman, ACS Appl. Mater. Interfaces, 6 (2014) 22192-22198.
[10] R.L. Hoye, R.E. Brandt, Y. Ievskaya, S. Heffernan, K.P. Musselman, T. Buonassisi, J.L. MacManus-Driscoll, APL Mater., 3 (2015) 020901.
[11] T. Minami, Y. Nishi, T. Miyata, Thin Solid Films, 549 (2013) 65-69.
[12] T. Minami, Y. Nishi, T. Miyata, Appl. Phys. Express, 8 (2015) 022301.
[13] t.
[14] Y.S. Lee, D. Chua, R.E. Brandt, S.C. Siah, J.V. Li, J.P. Mailoa, S.W. Lee, R.G. Gordon, T. Buonassisi, Adv. Mater., 26 (2014) 4704-4710.
[15] J.J. Loferski, J. Appl. Phys., 27 (1956) 777-784.
[16] A. Mittiga, E. Salza, F. Sarto, M. Tucci, R. Vasanthi, Appl. Phys. Lett., 88 (2006) 163502.
[17] A.T. Marin, K.P. Musselman, J.L. MacManus-Driscoll, J. Appl. Phys., 113 (2013) 144502.
[18] K. Musselman, Y. Ievskaya, J.L. MacManus-Driscoll, Appl. Phys. Lett., 101 (2012) 253503.
[19] A. Polman, H.A. Atwater, Nat. Mater., 11 (2012) 174.
[20] S.W. Lee, Y.S. Lee, J. Heo, S.C. Siah, D. Chua, R.E. Brandt, S.B. Kim, J.P. Mailoa, T. Buonassisi, R.G. Gordon, Adv. Energy Mater., 4 (2014) 1301916.

[21] J. Gan, S. Gorantla, H.N. Riise, Ø.S. Fjellvåg, S. Diplas, O.M. Løvvik, B.G. Svensson, E.V. Monakhov, A.E. Gunnæs, Appl. Phys. Lett., 108 (2016) 152110.
[22] B.M. Fariza, J. Sasano, T. Shinagawa, H. Nakano, S. Watase, M. Izaki, J. Electrochem. Soc., 158 (2011) D621-D625.
[23] S.-M. Chou, M.-H. Hon, C. Leu, Y.-H. Lee, J. Electrochem. Soc., 155 (2008) H923-H928.
[24] F. Biccari, University of Rome2012.
[25] A. Soon, X.-Y. Cui, B. Delley, S.-H. Wei, C. Stampfl, Phys. Rev. B, 79 (2009) 035205.
[26] Y.S. Lee, J. Heo, M.T. Winkler, S.C. Siah, S.B. Kim, R.G. Gordon, T. Buonassisi, J. Mater. Chem. A, 1 (2013) 15416-15422.
[27] K. Bergum, H.N. Riise, S. Gorantla, P.F. Lindberg, I.J. Jensen, A.E. Gunnæs, A. Galeckas, S. Diplas, B.G. Svensson, E. Monakhov, J. Phys. Condens. Matter, 30 (2018) 075702.
[28] Y. Liu, H.K. Turley, J.R. Tumbleston, E.T. Samulski, R. Lopez, Appl. Phys. Lett., 98 (2011) 162105.
[29] P. Viktorovitch, G. Moddel, J. Appl. Phys., 51 (1980) 4847-4854.
[30] J. Kneisel, K. Siemer, I. Luck, D. Bräunig, J. Appl. Phys., 88 (2000) 5474-5481.
[31] S. Johansson, M. Berg, K.-M. Persson, E.J. Lind, IEEE Trans. Electron Devices, 60 (2013) 776-781.
[32] Y. Yuan, L. Wang, B. Yu, B. Shin, J. Ahn, P.C. McIntyre, P.M. Asbeck, M.J. Rodwell, Y. Taur, IEEE Electron Device Letters, 32 (2011) 485-487.
[33] A. Marin, University of Cambridge2013.
[34] J. Gan, A. Galeckas, V. Venkatachalapathy, H.N. Riise, B.G. Svensson, E.V. Monakhov, MRS Online Proceedings, 1792 (2015).
[35] L. Papadimitriou, Solid-State Electron., 36 (1993) 431-434.
[36] M. Burgelman, P. Nollet, S. Degrave, Thin Solid Films, 361 (2000) 527-532.
[37] R.L. Hoye, B. Ehrler, M.L. Böhm, D. Muñoz-Rojas, R.M. Altamimi, A.Y. Alyamani, Y. Vaynzof, A. Sadhanala, G. Ercolano, N.C. Greenham, Adv. Energy Mater., 4 (2014) 1301544.

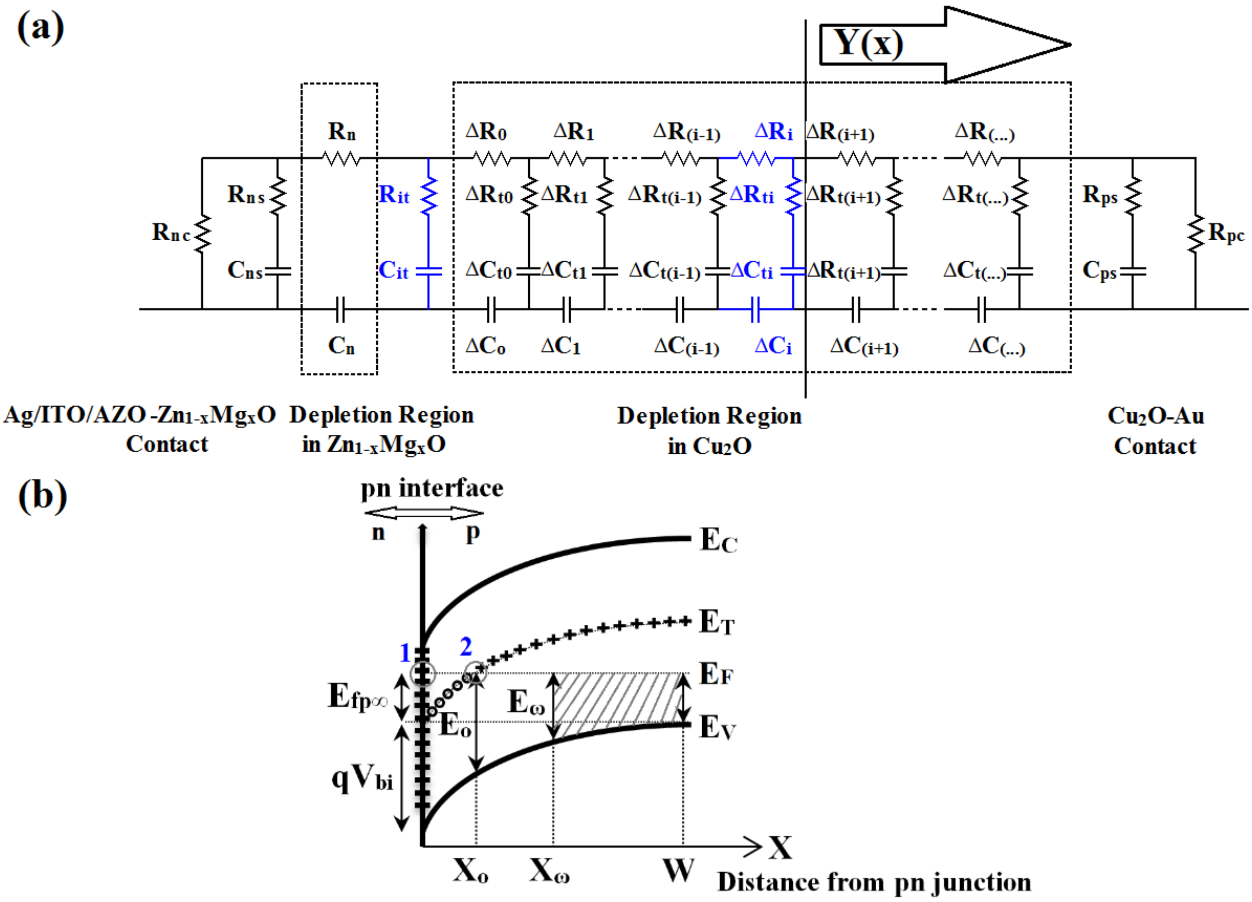

Figure 1. (a) An equivalent lumped resistor-capacitor (RC) circuit that represents the $Cu_2O/Zn_{0.8}Mg_{0.2}O$ p-n junction, including two metal-semiconductor junctions. ΔR_i and ΔC_i are the geometry related resistance and capacitance, while ΔR_{ti} and ΔC_{ti} are dynamic ones, which are related to the defects in Cu_2O or at interface. (b) Schematic of band diagram for $Zn_{0.8}Mg_{0.2}O/Cu_2O$ abrupt heterojunction. Numbers 1 and 2 in blue are used to denote the cross-section points of Fermi level (E_F) with interface defects and bulk defect level (E_T), respectively. Figure 1b is reproduced with permission.[17] Copyright 2013, American Institute of Physics.

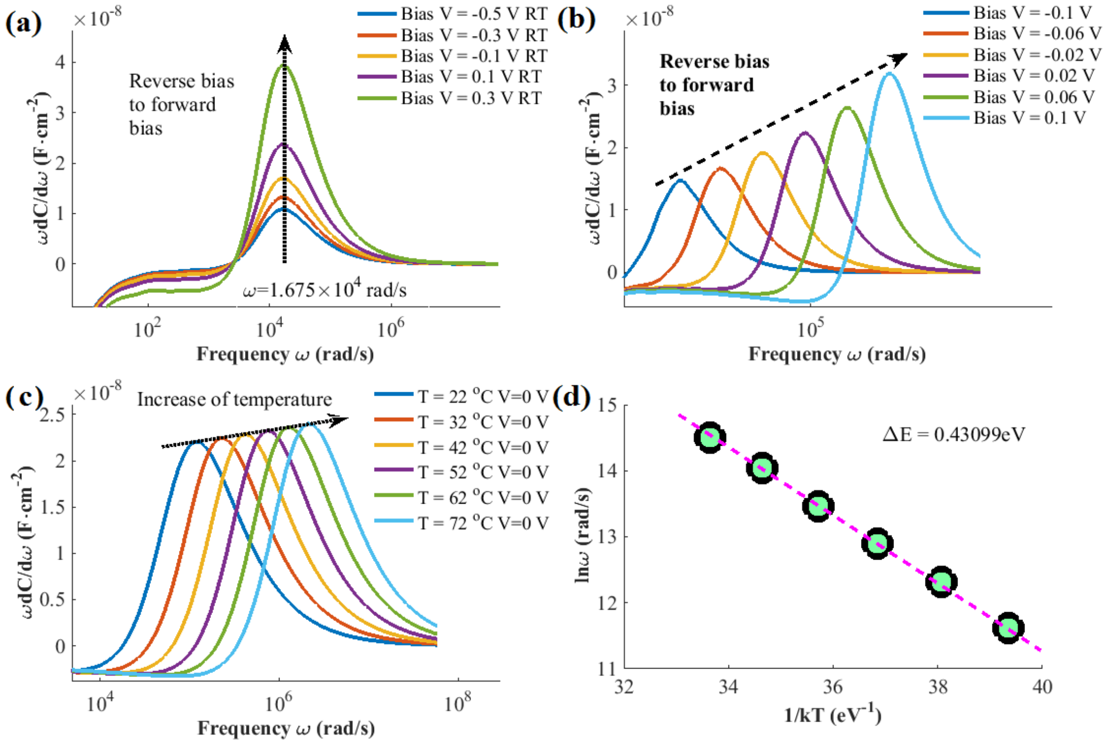

Figure 2. (a) Differential capacitance $\omega{\cdot}\mathrm{d}C/\mathrm{d}\omega$ with respect to angular frequency ω under different bias conditions from –0.5 V to 0.5 V from numerical results in Eq.6 to analyze bulk defects. The bias at 0.5 V did not give any result in the plot, the reason of the plot measured at forward 0.5 V is missing is because the probing energy E_ω at the highest frequency is smaller than E_{VF}). (b) Differential capacitance $\omega{\cdot}\mathrm{d}C/\mathrm{d}\omega$ with respect to angular frequency ω under different bias conditions from –0.1 V to 0.1 V from simulation to analyze interface defects. (c) Differential capacitance $\omega{\cdot}\mathrm{d}C/\mathrm{d}\omega$ with respect to angular frequency ω under different temperatures from 22 ºC to 72 ºC from simulation to analyze bulk defects (d) Extraction of the trap energy ΔE_o from shifts of $\omega{\cdot}\mathrm{d}C/\mathrm{d}\omega$ peaks with temperatures from Figure 2c.

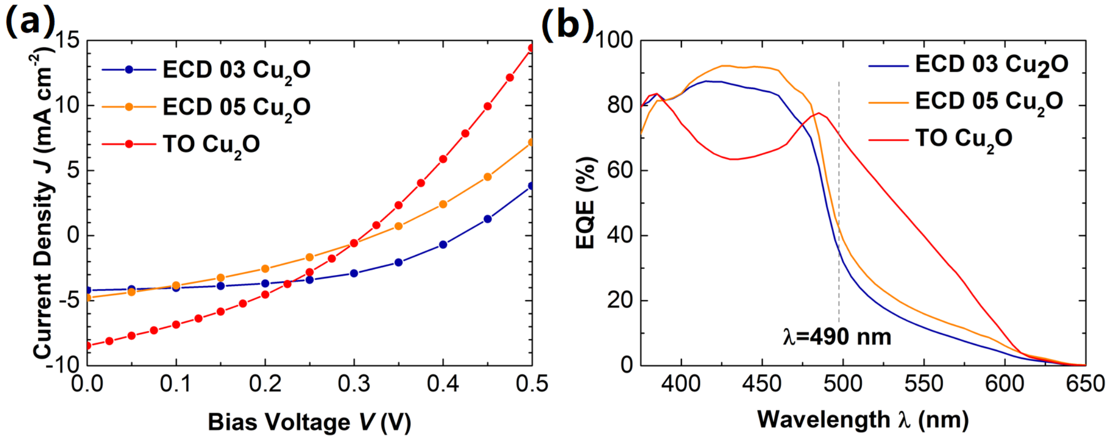

Figure 3. (a) Plots of current density versus bias voltage (*J*–*V*) for both types of samples under illumination of AM 1.5G radiation. (b) Plots of external quantum efficiency (EQE) for both types of samples.

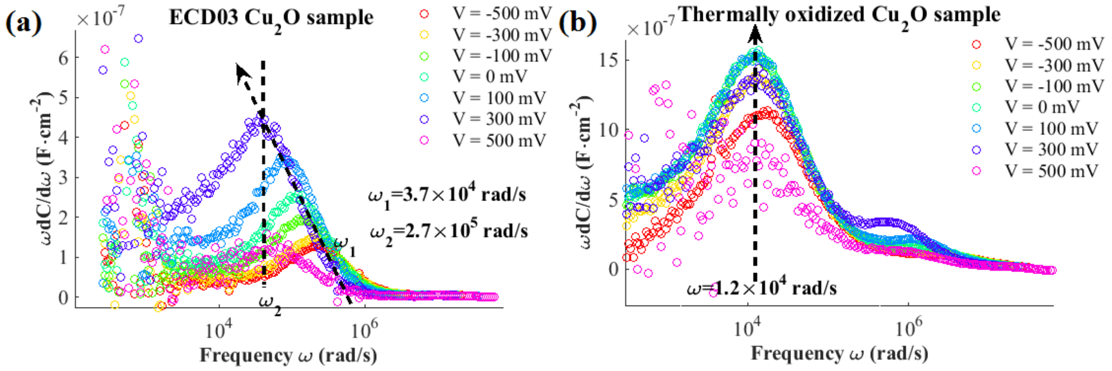

Figure 4. Differential capacitance $\omega \cdot dC/d\omega$ plots against angular frequency ω (a) ECD Cu_2O with $Zn_{0.8}Mg_{0.2}O$ deposited at 80 ºC (ECD03) and (b) thermally oxidized Cu_2O, under different bias conditions at room temperature.

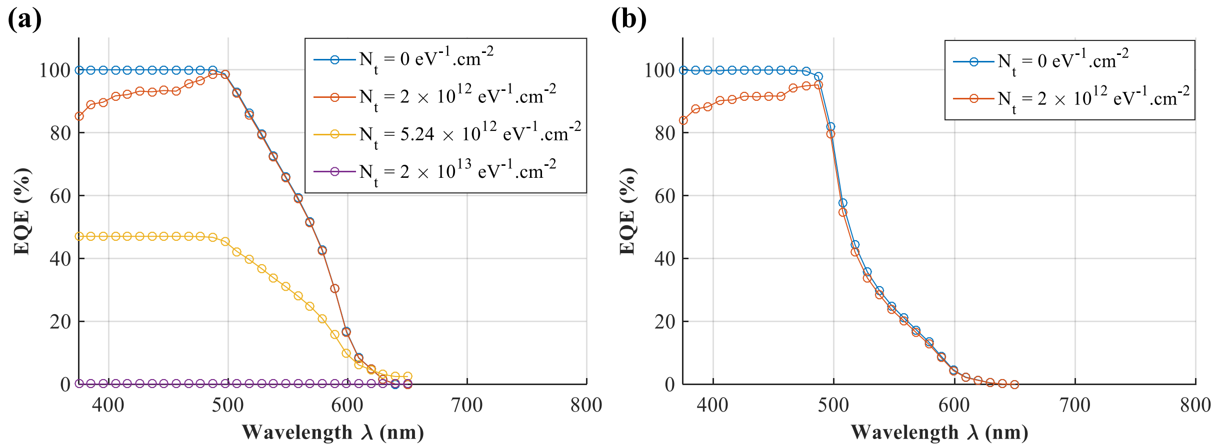

Figure 5. External quantum efficiency (EQE) of (a) thermally oxidized and (b) ECD Cu_2O devices calculated using SCAPS numerical simulation for different trap densities. The thermally oxidized Cu_2O was modeled with only interfacial recombination, with the defects having a Gaussian distribution located 0.5 eV above E_V. The ECD Cu_2O was modeled with a Gaussian distribution of bulk defects located 0.46 eV above E_V. The capture cross-section was taken as 4.5×10^{-12}, based on previous measurements.[17]

Table 1. Results of the peak maximum (lnω_o and kT^{-1}) at each temperature for bulk traps.

	T (K)					
	297	307	317	327	337	347
kT^{-1} (eV^{-1})	39.4	38.1	36.9	35.7	34.7	33.6
lnω_o (rad·s^{-1})	11.6	12.3	12.9	13.5	14.0	14.5
ω_o (rad·s^{-1})	1.2×10^5	2.4×10^5	4.2×10^5	7.5×10^5	1.3×10^6	2.1×10^6

Table 2. Parameters extracted from the *J–V* measurements for the two types of $Cu_2O/Zn_{0.8}Mg_{0.2}O$ heterojunction solar cells.

Samples	$Zn_xMg_{1-x}O$ deposition temperature (ºC)	V_{OC} [V]	J_{SC} [mA·cm^{-2}]	FF [%]	η [%]
ECD03 Cu_2O	80	0.43	4.4	53	1.02
ECD05 Cu_2O	150	0.33	5.0	34	0.55
TO Cu_2O	150	0.34	8.5	35	1